nature communications

Article

https://doi.org/10.1038/s41467-025-59726-x

Seamless incorporation of artificial water channels in defect-free polyamide membrane for desalination of brackish water

Received: 29 September 2024

Accepted: 30 April 2025

Published online: 13 May 2025

Check for updates

Yingsong Liu[1], Xieyang Xu[1], Chenshuo Wang[1], Huijun Yu[1], Weiyi Wang[1], Yanxi Gong[1], Changwei Zhao[2] & Jianbing Wang[1,3]

Artificial water channels (AWCs) show the potential for overcoming the permeability-selectivity tradeoff of polyamide (PA) membranes. However, the availability of biomimetic materials and limitations posed by fabrication-induced defects make the development of AWC-PA membranes a daunting task. Herein, we synthesize imidazolylethyl-ureidoethyl-phenyl (IUP) compounds to form AWC by self-assembling and provide a strategy to seamlessly incorporate AWC in defect-free PA membranes. IUP compounds are molecularly designed with enhanced nature to form AWC due to π-π stacking interactions. In addition, nanosized colloid AWC aggregates can be obtained in water directly with the aid of sodium dodecyl sulfate (SDS) and conveniently incorporated into PA layers. The AWC not only promotes the preferential selective passage of water but also exhibits good compatibility with the surrounding PA matrix. The biomimetic membranes demonstrate a water permeance of 4.3 $L \cdot m^{-2} \cdot h^{-1} \cdot bar^{-1}$ and NaCl rejection of 99.3%, much higher than that observed with marketed state-of-the-art membranes. Mechanism understanding reveals that the compatible interaction between AWC, SDS and PA matrix is a necessary requisite to fabricate defect-free AWC-PA layers. This strategy can be easily extended to industrial scale and the biomimetic membranes may represent the development direction of the next generation of high-performance reverse osmosis membranes.

Thin-film composite (TFC) polyamide (PA) membranes have been used in the desalination industry for more than 30 years[1]. The PA active layer are typically fabricated by interfacial polymerization (IP) of an amine monomer [e.g., m-phenylenediamine (MPD)] and an acyl chloride monomer [e.g., trimesoyl chloride (TMC)] at the interface of an aqueous solution and an organic solution[2]. Although the development of TFC-PA membranes represented a breakthrough for desalination, they still faced the limitation imposed by the permeability-selectivity tradeoff in the last decades[3].

In recent years, there has been potential for overcoming this limitation through the use of novel materials, such as nanotubes[4], laminated nanosheets[5,6], and nanoporous particles[7,8]. However, most nanomaterials are not capable of the selective rejection of ions. Parallel to these investigations, synthetic biomimetic artificial water channels (AWCs) have been proposed, including dendritic dipeptides[9], I-quartet[10], pillar[5]arene[11] and other foldamers[12–15] to control water translocation and prohibit ion insertion/translocation via synergetic donor-acceptor bonding[16]. However, the incorporation of AWCs into TFC-PA membranes was rarely reported, and it is a great challenge to incorporate the AWCs into a defect-free PA layer. Firstly, most AWCs were prepared through complex procedures, and it is not easy to obtain large quantities of nanosized AWCs. Secondly, due to the lack of

[1]School of Chemical and Environmental Engineering, China University of Mining and Technology-Beijing, Beijing, China. [2]College of Resources and Environmental Sciences, China Agricultural University, Beijing, China. [3]National Key Laboratory of Coal Fine Exploration and Intelligent Development, China University of Mining and Technology-Beijing, Beijing, China. e-mail: wangjb@cumtb.edu.cn

stabilizing interactions between some AWCs and PA matrix, the immobilization of these novel materials in membrane matrices would be difficult, likely resulting in the generation of defects[17]. Then, some AWCs, such as I-quartet AWCs formed from supramolecular organization of alkylureido-ethylimidazole compounds (HC4, HC6, and HC8) were formed at the interface between water and organic solvent and cannot be directly added into the MPD aqueous solution or TMC organic solution[18]. In addition, the formation of nanosized AWC was sensitive to environmental conditions such as the ethanol/water ratio and the concentration of HCs in ethanolic solution[17]. Therefore, high levels of control over environmental conditions were required to obtain nanosized AWCs, incorporate them into the PA layer, avoid defect generation, and optimize the performance of the AWC-PA layer. A possible strategy is to design AWC with intrinsic properties whose nanoaggregates can be directly obtained in water systems and explore an easy fabrication strategy to prepare a defect-free PA membrane and realize the scale of biomimetic membranes for industrial standards. Also, mechanistic understanding of fabrication strategy is significant to prepare a defect-free PA membrane.

Herein, we reported an AWC formed from supramolecular organization of imidazolylethyl-ureidoethyl-phenyl (IUP) compound and an easily scaled fabrication strategy of biomimetic AWC-PA membrane. IUP compounds were molecularly designed to realize their dissolution in water, and the direct obtainment of nanosized colloid AWC aggregates in water with the proper use of sodium dodecyl sulfate (SDS) was also investigated. The proposed strategy allows seamless incorporation of AWC into the PA layer and stable fabrication of defect-free AWC-PA membrane exhibiting high water permeance and salt rejection. In addition, mechanistic understanding related to the strategy was undertaken to give an insight into the effect of colloid AWC aggregate formation on defect generation during the incorporation of AWC into the PA layer and the interactions between AWC, SDS, and PA matrix on the performance of biomimetic membranes.

Results

Structure and function of AWC formed by the self-assemble of IUP

Inspired by the structure of the Aquaporin (AQP)[2], we designed an artificial water channel (AWC) formed from supramolecular organization of IUP compounds by means of urea groups. During the supramolecular organization, both the hydrophilic and hydrophobic portions in IUP compounds can be harmonized so that they are oriented in the same direction to form AWC crystals. The structure of IUP is believed to be favorable for the formation of nanosized AWC aggregates in water due to its molecular chain length, phenyl group and π-π stacking interactions (Fig. 1a–d). Furthermore, π-π stacking enhances the compatibility between AWC and PA matrix (vide infra). The design philosophy of AWC is listed in the Supplementary Information.

The IUP compound was synthesized via a single-step reaction between histamine and phenylethyl isocyanate. The white powder of the IUP compound was readily available in the synthesis experiment and subjected to nuclear magnetic resonance (NMR) analysis (Supplementary Figs. 1 and 2). The results validated the chemical structure of the IUP molecules (Fig. 1a). The single crystal X-ray diffraction analysis revealed the expected structure of the IUP I-quartet containing oriented water-wires. The pore size of the channels between four imidazole groups is ~2.6–2.8 Å (Fig. 1c). The channels containing water wires with the opposite dipole orientations are essential for AWC to provide the water translocation function (Fig. 1d). The AWC crystal structure exhibits slipped π−π interactions between the benzene rings of neighboring IUP molecules [centroid-centroid distance = 4.619 Å, perpendicular distance = 3.764 Å, and slippage = 2.677 Å] (Supplementary Fig. 5). Based on the structure, we concluded the existence of π-π stacking facilitates supramolecular self-assembly[19,20], thereby supporting the enhancement of AWC formation in aqueous solution in this study.

We performed molecular dynamics (MD) simulation of water transport with an AWC slice containing 12 water wires. Under the pressure exerted by the graphene piston, water molecules in the brine chamber were driven into the freshwater chamber through the AWC slice (Fig. 1e), while Na^+ and Cl^- were completely rejected by the water channel (Supplementary Fig. 38). Water conductance was positively correlated with the applied pressure (Supplementary Fig. 39), and the average permeability of the water channel was 3.59×10^6 H_2O/channel/s/bar (Fig. 1f). According to the MD simulation, we obtained the radial distribution function (RDF) between the H2 atom in the IUP molecules and the O atom in the water molecules. There were two peaks at ~2.1 Å and 3.2 Å, respectively. This indicates a H2 atom of the IUP molecule formed a hydrogen bond with the O atom of the H_2O molecule with the distance of 2.1 Å, and it was 3.2 Å away from the O atom of the two neighboring water molecules (Fig. 1g). In addition, the distance between them can take a value ranging from 2.1 to 3.2 Å, indicating the jumping activity of water molecules in channels[21]. The water permeability of AWC in liposomes was tested using D(+)-sucrose as a penetrating agent in a stop-flow apparatus (methods see Supplementary Information). When the molar ratio of IUP to lipid was 0.2862, the net permeability by channels in liposomes was 75.00 μm/s (Supplementary Fig. 19). The calculated single-channel permeability of AWC was 5.79×10^7 H_2O/s/channel in the lipid bilayer membrane. The AWC formed from IUP compounds demonstrated comparable water translocation performance to the other type of AWC (~10^6 H_2O/s/channel) observed in the previous study[10].

Biomimetic AWC membrane for reverse osmosis desalination

Our fabrication strategy is first to disperse AWC aggregates formed in water containing MPD and SDS onto a commercial polysulfone (PSf) support and then to conduct an IP procedure for realizing the incorporation of AWC aggregates and preparation of AWC-SDS-PA membrane (Fig. 2a). Briefly, IUP compound, MPD, and SDS were dissolved in water using heating and ultrasound. After cooling, nanosized colloid AWC aggregates were formed in the water, and the resultant aqueous solution was used to begin IP with TMC hexane solution. In particular, SDS was used to regulate the formation of colloid AWC aggregates due to its excellent dispersion effect as a surfactant[22]. For comparison, we fabricated AWC-PA membranes first by dissolving IUP in ethanol and then adding water into ethanol to obtain nanosized colloid AWC aggregates which were finally dispersed onto the surface of PSf support before starting the traditional IP procedure. Also, we used conventional IP procedures to fabricate the SDS-PA and PA membranes, respectively.

Scanning electron microscopy (SEM) micrographs (Supplementary Figs. 21–23) show that the extensive irregular and crumpled structures of both SDS-PA and AWC-SDS-PA membranes differed from those of PA membranes. This may be due to the reduced interfacial tension between hexane and aqueous solution caused by SDS[23]. The cross-sectional transmission electron microscopy (TEM) images of the membranes showed the dark stripes representing the PA layer (Fig. 3), and the toothing of the stripes corresponding to the ridge-and-valley-like morphology of the PA layer[24]. Some bright spots were observed in the TEM images of both AWC-PA and AWC-SDS-PA membranes. The bright spots could correspond to the AWC aggregates in the PA layer as indicated in literature[25], and the incorporation of AWC aggregates with molecular regularity into the PA layer was confirmed by the Cryo-transmission electron microscopy (cryo-TEM) and XRD analysis (Supplementary Figs. 26 and 27, Supplementary Movies 1–3). By analyzing the size of bright spots in the TEM images, it can be concluded that the AWC aggregates in the AWC-SDS-PA membranes presented a smaller size than those in AWC-PA membranes, indicating that the addition of SDS reduced the size of the AWC aggregates and enhanced their

dispersion in the PA layer. Some AWC aggregates were not fully encapsulated by the PA layer of AWC-PA membranes, while the PA layer of AWC-SDS-PA membranes completely encapsulated all AWC aggregates. The stripe width in the TEM images of the PA, AWC-PA, SDS-PA, and AWC-SDS-PA membranes were ~80 nm, 120 nm, 220 nm and 260 nm, respectively (Fig. 3). The analysis of the atomic force microscopy (AFM) images showed the PA layer thickness was about 47 nm, 89 nm, 146 nm and 214 nm, respectively (Supplementary Fig. 24). These results suggest the incorporation of AWC and use of SDS resulted in a thicker PA layer.

The X-ray photoelectron spectroscopy (XPS) analysis showed that the nitrogen (N) and oxygen (O) contents of the SDS-PA membranes were similar to those of the control membranes (Supplementary Fig. 28), indicating the addition of SDS posed a negligible effect on the elemental composition of the PA layer. The O/N ratio of the membranes was about 1.25 due to the hydrolysis of unreacted acyl chloride groups to carboxyl groups[26]. Compared to the control membranes, the O/N ratios of the AWC-PA and AWC-SDS-PA membranes decreased to 0.85 and 1.08, respectively (Supplementary Table 2). Reminiscent of the IUP chemical formula ($C_{14}H_{18}N_4O$), the decrease in the O/N ratio indicates the incorporation of AWC aggregates.

We tested the separation performance of various membranes in a reverse osmosis system with an operating pressure of 16 bar for the desalination of mimicked brackish water. Obviously, the SDS-PA membranes provide a consistent increase in water flux and salt rejection compared to the control membranes (Fig. 4a). The average water permeance and salt rejection of the optimized SDS-PA membrane are 2.1 $L \cdot m^{-2} \cdot h^{-1} \cdot bar^{-1}$ and 98.8%, respectively. The AWC-PA membranes presented erratic performance and hardly displayed both high permeability and selectivity (Fig. 4b). When the IUP concentration in the ethanolic solution was 4%, the water permeability was 2.2 $L \cdot m^{-2} \cdot h^{-1} \cdot bar^{-1}$, while the salt rejection decreased to 88.5%.

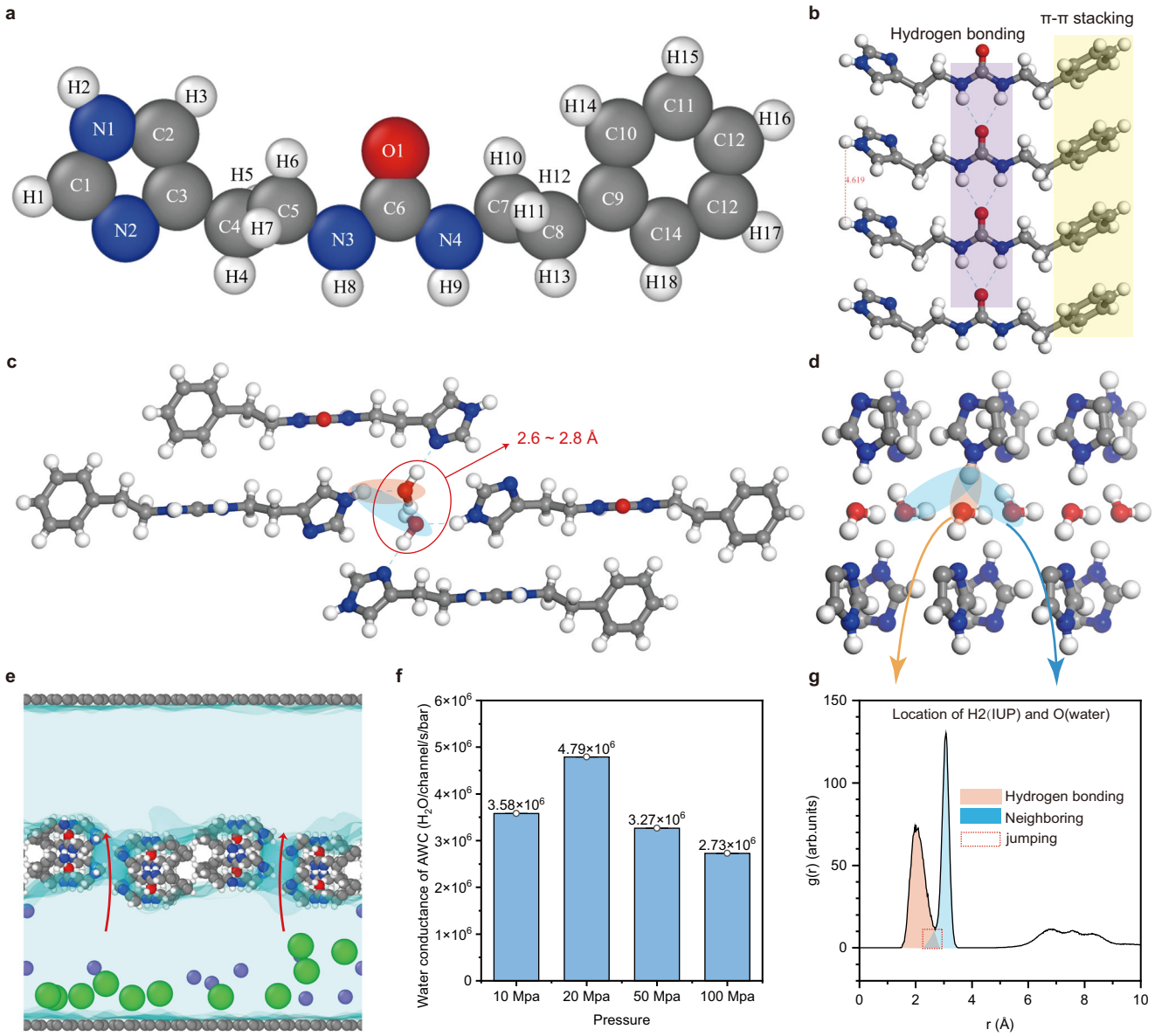

Fig. 1 | Structure of AWC formed from self-assemble of IUP compound and results from MD simulation of water transport in AWC. a Chemical structures of IUP compounds. **b** IUP intermolecular interactions in AWC crystals. The distance between IUP molecules is 4.619 Å. Structure of the water channel in the AWC crystal is shown in top view (**c**) and side view (**d**). Two types of hydrogen bonds are highlighted in yellow and blue, respectively. **e** MD simulation for the movement of water molecules in an AWC crystal with light blue for water molecules, purple for sodium ions, and green for chloride ions. **f** Single-channel permeability of AWC in the lipid bilayer membrane. **g** Radial distribution function (RDF) between the H2 atom in the IUP molecules and the O atom in the water molecules.

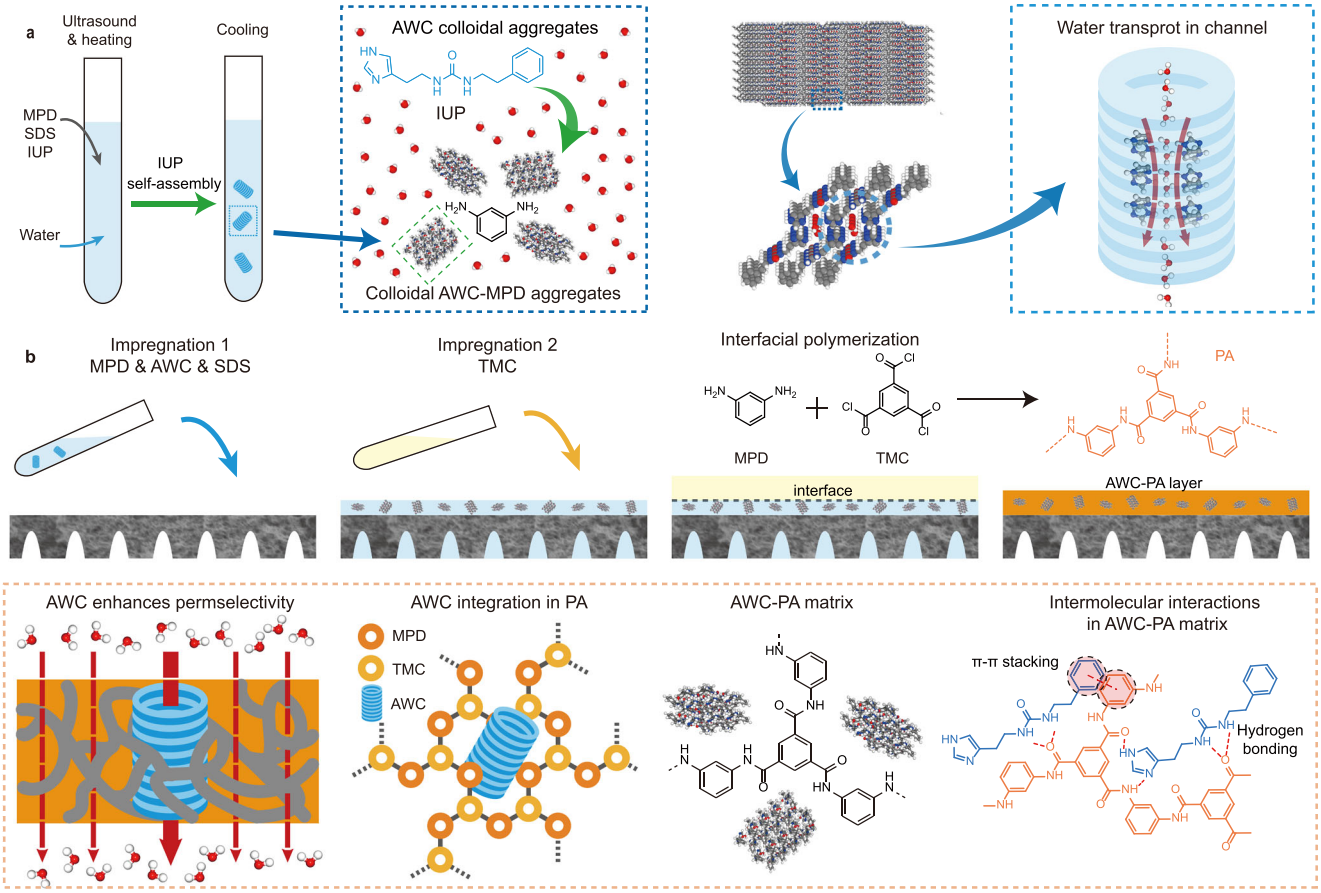

Fig. 2 | Schematic diagram of preparing AWC-SDS-PA membrane and hypothetical mechanism. a Obtainment of colloid AWC aggregates by mixing IUP, SDS, and MPD in water, followed by the treatment of heating, ultrasound, and cooling. **b** Impregnation 1 of the PSf ultrafiltration support with an aqueous solution of IUP, SDS, and MPD, followed by impregnation 2 with a hexane solution of TMC to begin IP to prepare the composite PA TFC-IUP membranes incorporating AWCs.

This was ascribed to the uncertainty of AWC aggregate formation and the probability of defect formation in AWC-PA membranes.

The AWC-SDS-PA membranes obviously displayed a better combination of water permeance and salt rejection compared to both the control membranes and SDS-PA membranes (Fig. 4c). As the concentration of IUP increased to 0.1%, while keeping the MPD concentration constant [2.0% (wt/vol)], the water permeance of the AWC-SDS-PA membranes continuously increased with a slight change in salt rejection (Fig. 4c). This indicates that almost no detrimental defects were generated in the AWC-SDS-PA membrane with the IUP concentration less than 0.1%. Above the IUP concentration of 0.1%, a decrease in permeance was observed. This phenomenon is explained by the reduction of AWC incorporated into the PA layer and the increasing of the defect generation probability in the PA layer (vide infra). A definite or mathematical explanation cannot be provided due to the uncertain effect of the IUP concentration on membrane performance, also indicated by the increased error bars related to the performance of the membranes fabricated with the IUP concentration of 0.8%.

The average water permeance and salt rejection of the optimized AWC-SDS-PA membranes were 4.3 $L \cdot m^{-2} \cdot h^{-1} \cdot bar^{-1}$ and 99.3%, respectively, providing a better combination of water permeance and salt rejection compared to the marketed state-of-the-art membranes (Fig. 4d). They also displayed obviously higher water permeance and little change in solute permeability coefficient compared to the control membranes. The improvement of water permeability for the AWC-SDS-PA membrane was also verified by the estimation with Maxwell equation (details of estimation see Supplementary Information section 10). The associated data of permeability-selectivity performance beyond the bound line indicates that the optimized AWC-SDS-PA membranes defeated the selectivity-permeance trade-off (Fig. 4e). AWC-SDS-PA membranes also had higher permselectivity (Fig. 4f) than the membranes reported in previous studies[8,27–33].

Mechanistic understanding of the formation of AWC aggregates and its incorporation influencing the performance of TFC-IUP membranes

To understand the kinetic formation of AWC aggregates in various systems, we measured the hydrodynamic diameters (D_h) of colloidal AWC aggregates by dynamic light scattering (DLS) analysis. After water was added to 1 mL of IUP ethanolic solution, AWC aggregates (D_h = 176–740 nm) were immediately formed. Environmental conditions posed a cross-effect on the formation of AWC aggregates. First, the D_h values increased with the concentration of IUP (Fig. 5a). Secondly, the D_h values first increased and then decreased with the water/ethanol ratio ranging from 0.2 to 5 (Fig. 5a). The continuous addition of water to ethanol hardly reduced the D_h values below 200 nm (Fig. 5b, c). Then, the mixing way and strength of water and ethanol and self-assembly time had a significant impact on the D_h values (Supplementary Figs. 10–14). Therefore, we believe the difficulty in regulating the formation of AWC aggregates by adding water into the ethanolic solution of IUP is the main reason for the erratic performance of the AWC-PA membranes.

IUP can be directly dissolved in water by heating and ultrasound. We added SDS into water to prevent AWC from agglomeration, reminiscent of that surfactants enhanced the dispersion of

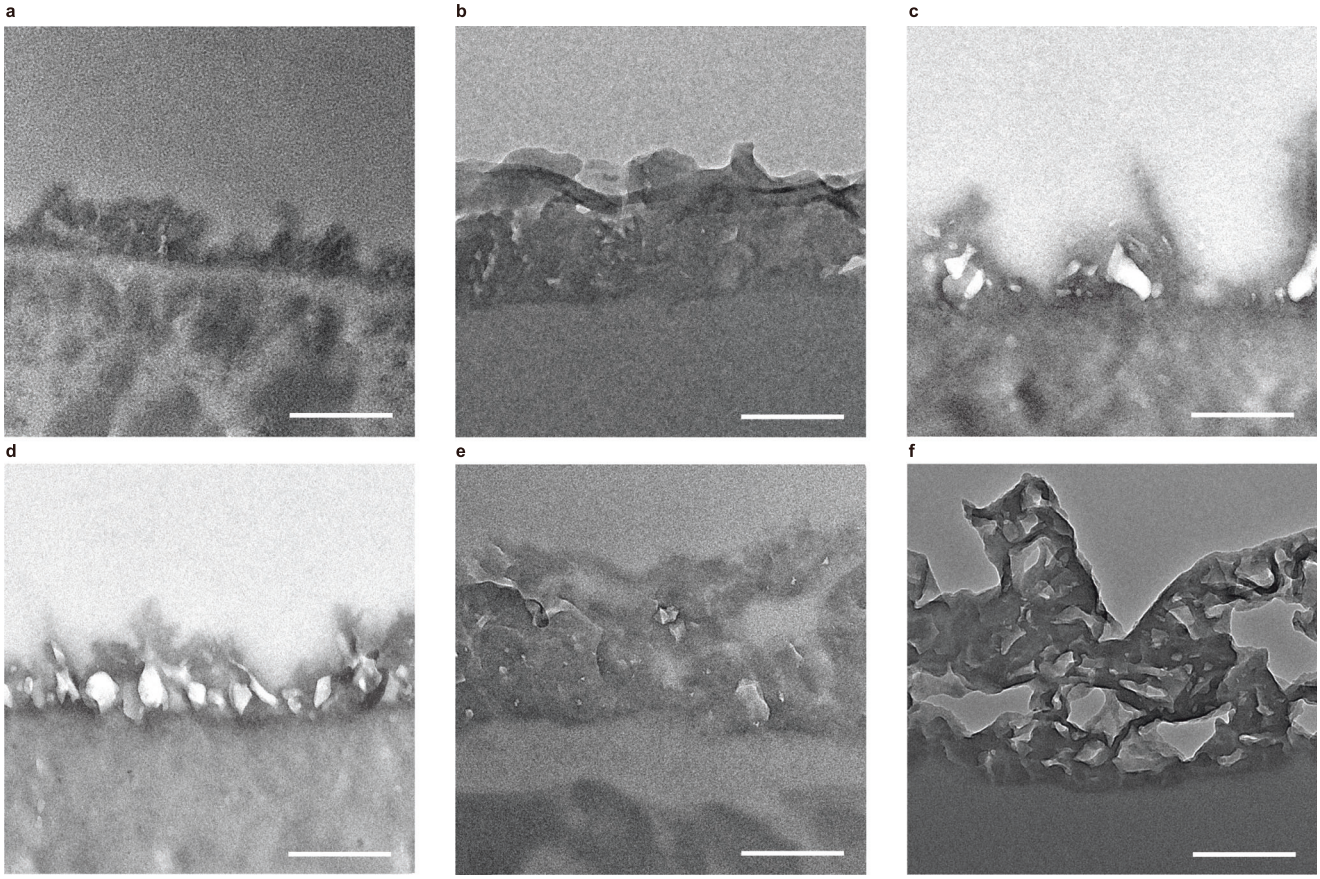

Fig. 3 | Morphological TEM characterization of the membranes. The TEM cross-sectional images show the PA layer on porous PSf support. The brighter spots could correspond to the AWC aggregates in the PA layer. Scale bar, 200 nm. **a** The control membrane. **b** SDS-PA membrane (SDS concentration is 0.2%). **c**, **d** AWC-PA membrane (IUP concentration in ethanol solution is 0.25% and 4.0%, respectively). **e**, **f** AWC-SDS-PA membrane (IUP concentration in water solution is 0.05% and 0.8%, respectively).

nanoparticles[34,35]. After cooling, colloidal AWC aggregates were formed, and the D_h values ranged from 40 to 120 nm (Fig. 5d). With the aid of SDS, the concentration of IUP can be increased to at least 1.0% without any precipitation formation. In addition, the D_h values decreased with the increasing SDS concentration, and they were reduced to about 50 nm with the SDS concentration of 0.2% (Fig. 5e). The addition of MPD to the solution resulted in the reduction of D_h values of colloidal AWC nanoaggregates (Fig. 5f). This may be attributed to the adsorption of MPD on the surface of AWC nanoaggregates, thereby preventing their aggregation. These nanosized AWC aggregates with a D_h of 50–100 nm can be highly dispersed and effectively incorporated into the PA layer, thereby reducing the probability of defect generation to a very small extent.

MD simulations showed that the water permeability (K_w) of the PA and the AWC-PA layers were 0.359×10^{-6} L·m^{-1}·h^{-1}·bar^{-1} and 0.827×10^{-6} L·m^{-1}·h^{-1}·bar^{-1}, respectively. The AWC aggregates increased the water permeability by 130%. In the AWC-PA layer, there are two types of water transport pathways, the internal channels of AWCs and the external channels between AWC aggregates and PA matrix (Supplementary Figs. 44 and 45, Supplementary Movies 4 and 5). Water transport substantially occurs in the internal channels of AWC, greatly improving the permselectivity through donor–acceptor H-bonding interactions. The external channels between AWC aggregates and PA matrix also facilitated the permeation of water molecules, while they had no selective mechanism for complete rejection of small ions. Too wide external channels may lead to a reduction in the salt rejection and be regarded as a kind of defect. The intermolecular force between the AWC aggregates and the PA matrix can reduce the width of the external channel. The total interaction energy and π−π stacking interaction energy between AWC aggregates and PA matrix in the AWC-PA model were calculated to be −342.7 kcal/mol and −71.4 kcal/mol, respectively (Supplementary Fig. 43). The π−π stacking interaction is an undeniable attractive force between AWC and PA matrix[36–38], strengthening their affinity and adhesion to reduce defect generation.

MD simulation also revealed the migration of AWC aggregates at the water-hexane interface. If given an initial velocity of Brownian motion as a result of the generated exothermic bubbles and turbulence, the AWC aggregates could enter into the organic phase during IP (Fig. 6a). Based on the close relationship between particle size and Brownian motion, it is speculated that AWC aggregates with large D_h values may have difficulty entering the organic phase. This can be used to explain why high concentrations of IUP led to a decrease in membrane performance. Due to the intermolecular hydrogen bond and π−π stacking interaction, the AWC aggregates could adsorb MPD, and both of them entered the organic phase together (Fig. 6b). When SDS was added to the MPD aqueous solution, dissociated dodecyl sulfate was formed at the water-hexane interface. The MD simulation showed the addition of SDS posed a negligible effect on the migration of AWC aggregates across the interface (Fig. 6c). It was also reported that the addition of SDS in the aqueous phase does not affect the diffusion of nanoparticles at the water-oil interface[39]. Experiments were conducted to evaluate the diffusion of MPD into the organic phase during IP at varying SDS concentrations. The results demonstrated that SDS facilitated the migration of MPD across the interface (Supplementary Fig. 48), resulting in the increase of PA layer thickness based on the finding of the previous study[40]. The thick PA layer can completely

https://doi.org/10.1038/s41467-025-59726-x

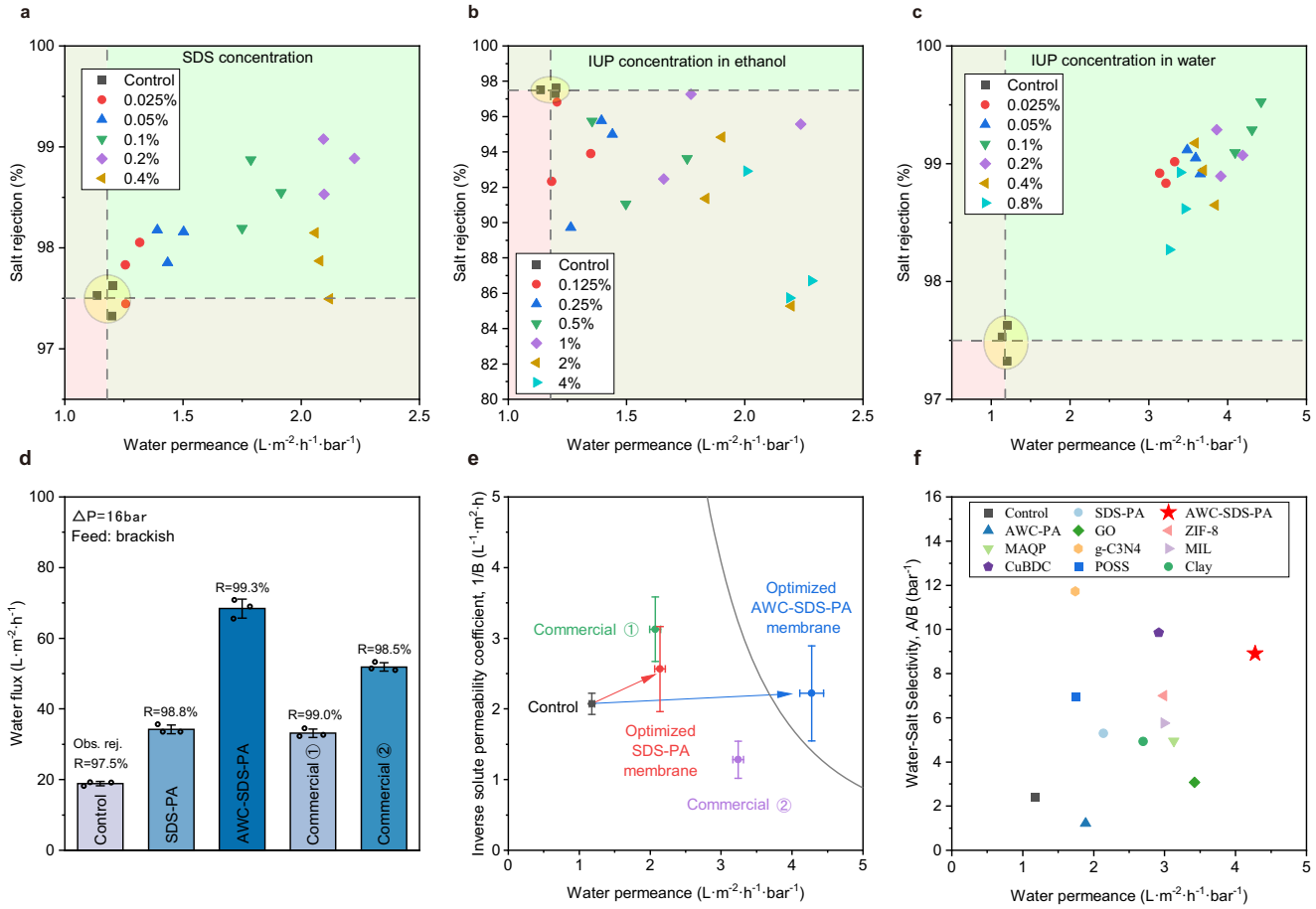

Fig. 4 | Performance of the membranes in the desalination of brackish water. Experimental water permeance and observed solute rejection of the control membranes, SDS-PA membranes (**a**), AWC-PA membranes (**b**), and AWC-SDS-PA membranes (**c**). The filtration conditions were: 16 bar applied pressure with 2000 ppm NaCl feed solution at pH 7.5 for brackish water desalination. **d** Experimental water flux and observed solute rejection of our membranes and commercial membranes (Obs. rej., observed rejection), data are presented as mean values ± SD, n = 3. **e** Permselectivity of optimized membranes and commercial membranes, data are presented as mean values ± SD, n = 3. **f** Water permeability and water-salt selectivity of membranes in this work and previous studies. Commercial membrane 1 and 2 are SW30 (Dupont) and BW30 (Dupont), respectively.

encapsulate AWC aggregates, reducing the probability of defect generation. In the system containing MPD, SDS and AWC aggregates, some AWC aggregates adsorbing MPD molecules entered the organic phase, while the dodecyl sulfate stayed at the interface (Fig. 6d). Their interaction is beneficial for increasing the thickness of the PA layer. As the reaction between MPD and TMC continued to occur, the associated AWC aggregates were integrated into the PA layer through the formation of a hybrid AWC/MPD nanoparticle. AWC-PA layers were continuously generated via the interaction of amphiphilic AWC/MPD nanoparticles with nascent PA oligomers via H-bonding and π-π stacking.

Discussion

According to the above results, the preparation of defect-free biomimetic membranes with excellent perm-selective behavior was successful due to the intrinsic nature of IUP with enhanced solubility and affinity to form AWC, highly selective AWC with excellent structural compatibility with the surrounding PA matrix, direct obtainment of nanosized AWC aggregates in water with the aid of SDS, and positive interactions between MPD, SDS and AWC during the incorporation of AWC into the PA layer.

While currently achievable in the laboratory, scaling up for commercial use is a daunting task. Currently, the limitations caused by fabrication-induced defects are still a critical limiting factor in the development of practical AWC-PA membranes. An easily scalable strategy for rational incorporation of AWC in a defect-free PA layer is very important for overcoming these defects, besides high levels of control over environmental conditions. In this study, IUP compounds were molecularly designed with easy availability at great production and enhanced intrinsic nature to form AWC. In addition, nanosized colloidal AWC aggregates can be directly obtained in aqueous solution with the help of SDS. When mixed with MPD aqueous solution, the colloidal AWC aggregates would still remain stable in aqueous solution with a smaller size. Therefore, we can conveniently use the aqueous solution containing both AWC, MPD and SDS to replace the MPD aqueous solution in industrial equipment for the preparation of practical AWC-PA membranes using conventional IP procedures (Supplementary Fig. 49). Additionally, a production line is built to obtain a large amount of IUP compounds, and a dissolving tank with heating, ultrasonic and cooling devices is necessary to obtain the aqueous solution containing MPD, SDS and colloid AWC aggregates. The aqueous solution in the tank can be directly introduced into the unit for the impregnation of MPD in the industrial production line. This indicates that the fabrication strategy proposed in this study can be easily extended to industrial standards without complicated equipment upgrading. The window for SDS concentration is relatively wide according to the results in this study, and the addition of SDS will not provide additional regulatory difficulties to the IP procedure. The rational seamless incorporation of AWC in a defect-free PA membrane provides an example of biomimetic AWC membranes applied under

https://doi.org/10.1038/s41467-025-59726-x

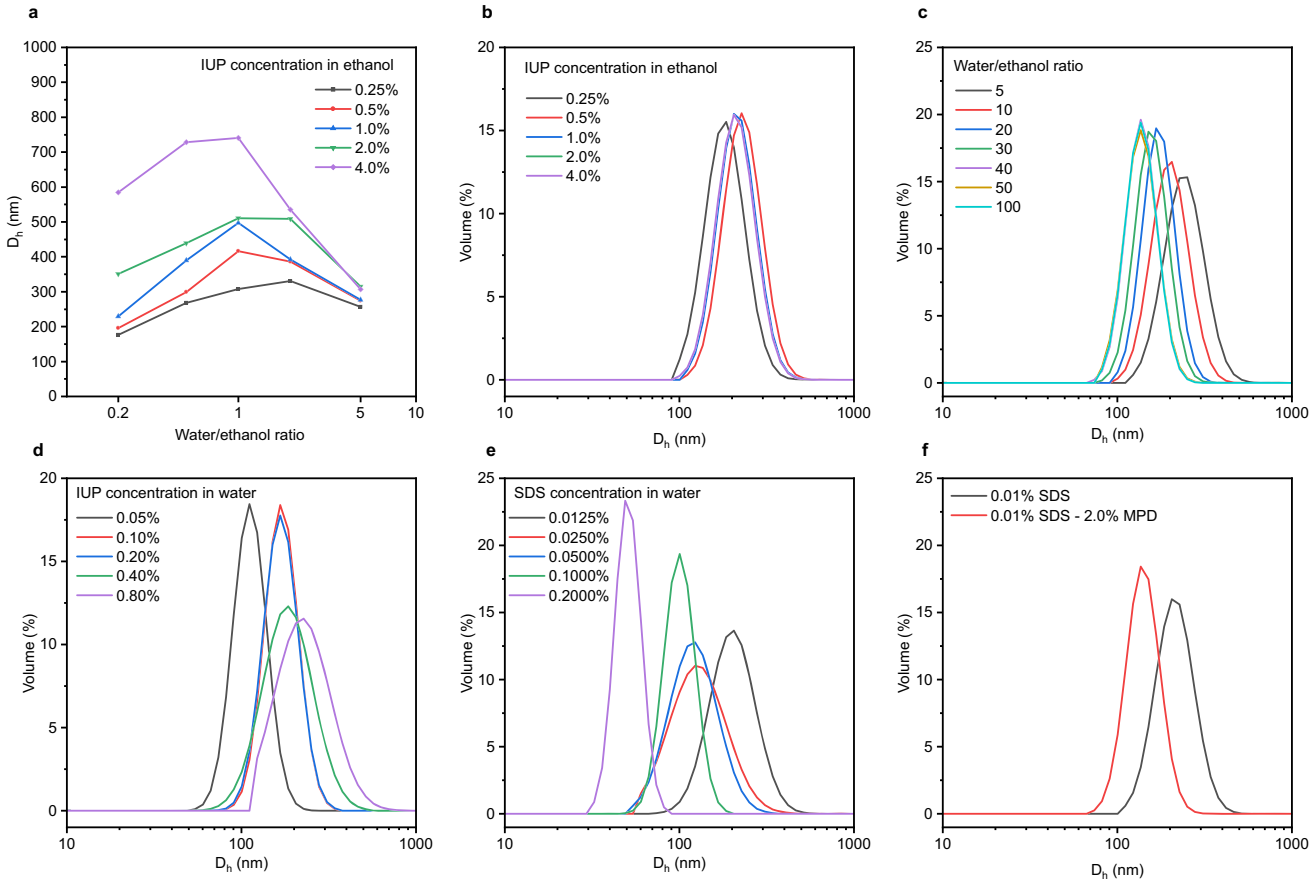

Fig. 5 | Dynamic light scattering (DLS) experiments of AWC aggregates in the ethanol-water system or water system. Colloidal AWC aggregates can be obtained by adding water to an IUP ethanolic solution. Measured D_h values for colloidal AWC aggregates formed by adding water into ethanoic solution of different IUP concentrations (**a**). Distribution of the D_h values for AWC aggregates formed at the ethanol/water ratio of 5 and IUP concentration ranging from 0.25% to 4.0% (**b**). Distribution of the D_h values for AWC aggregates formed by continuously adding water into an ethanolic solution of 4% (**c**). Colloidal AWC aggregates can be obtained in water solution. Distribution of the D_h values for colloid AWC aggregates formed in water at various IUP (**d**) and SDS (**e**) concentrations, and with/without the addition of MPD (**f**).

representative reverse osmosis desalination conditions with excellent perm-selective behavior. These biomimetic membranes could be easily scaled for industrial standards (>m^2), and may represent the development direction of the next generation of high-performance reverse osmosis membranes.

Methods

Synthesis of the IUP compounds

9.00 mmol of phenethyl isocyanate (1.25 mL) was prepared in a mixture of 10.0 mL of THF, 10.0 mL of ACN, and 5.00 mL of ethyl acetate. The corresponding equimolar amount of histamine (1.00 g) was then added to the reaction mixture, which was stirred and heated to 80 °C. The reaction was then condensed and refluxed for 3 h. As the reaction system warmed, the histamine was gradually dissolved. Upon completion of the reaction, a white precipitate (IUP) appeared in the flask. The solution is distilled in order to separate as many solvents as possible, and then cooled to room temperature. The white precipitate was obtained by vacuum filtration using a PTFE filter membrane and washed with hexane and filtered. The white precipitate was subjected to freeze-drying in order to remove the solvent, thereby producing 2.18 g of purified white powder product with a percent yield of 94.0%.

Membrane fabrication

TFC membrane were fabricated using traditional interface polymerization (IP) methods on microporous PSf substrates, designated as the control membrane. Specifically, a PSf substrate with a size of 10×13 cm^2 was adhered to a metal plate and then soaked in a 2.00 wt/vol% MPD aqueous solution for 2 min. Then the surface of the PSf substrate was wiped clean with a rubber roller to remove any residual water droplets. Subsequently, a 0.10 wt/vol% TMC n-hexane solution was poured on the membrane surface for 1 min. Then, the n-hexane solution was poured out. Subsequently, the surface of PA was cleaned with n-hexane in order to remove any residual TMC monomers. The reaction between MPD and TMC results in the formation of an ultra-thin PA selective layer. The TFC membrane was then removed from the metal plate and annealed in a 60 °C oven for 5 min. Finally, the membrane was repeatedly washed with deionized water and stored in deionized water until required.

The aqueous solution was subjected to the addition of SDS with varying concentrations, and the preparation of SDS-PA membranes was conducted in accordance with the established IP procedure. In order to integrate AWC aggregates into the PA layer, MPD aqueous solution was added to different concentrations of IUP ethanol solution in a ratio of 5:1 (water: ethanol) to obtain AWC aggregates, and AWC-PA membrane was prepared by the above IP procedure. For AWC-SDS-PA membrane, the IUP compound was first dissolved in an aqueous solution containing 2.00% MPD and 0.20% SDS by heating (60°C) and ultrasound. After the solution was cooled to room temperature, dispersed AWC aggregates were obtained. Then the AWC-SDS-PA membrane was prepared by the above IP procedure.

https://doi.org/10.1038/s41467-025-59726-x

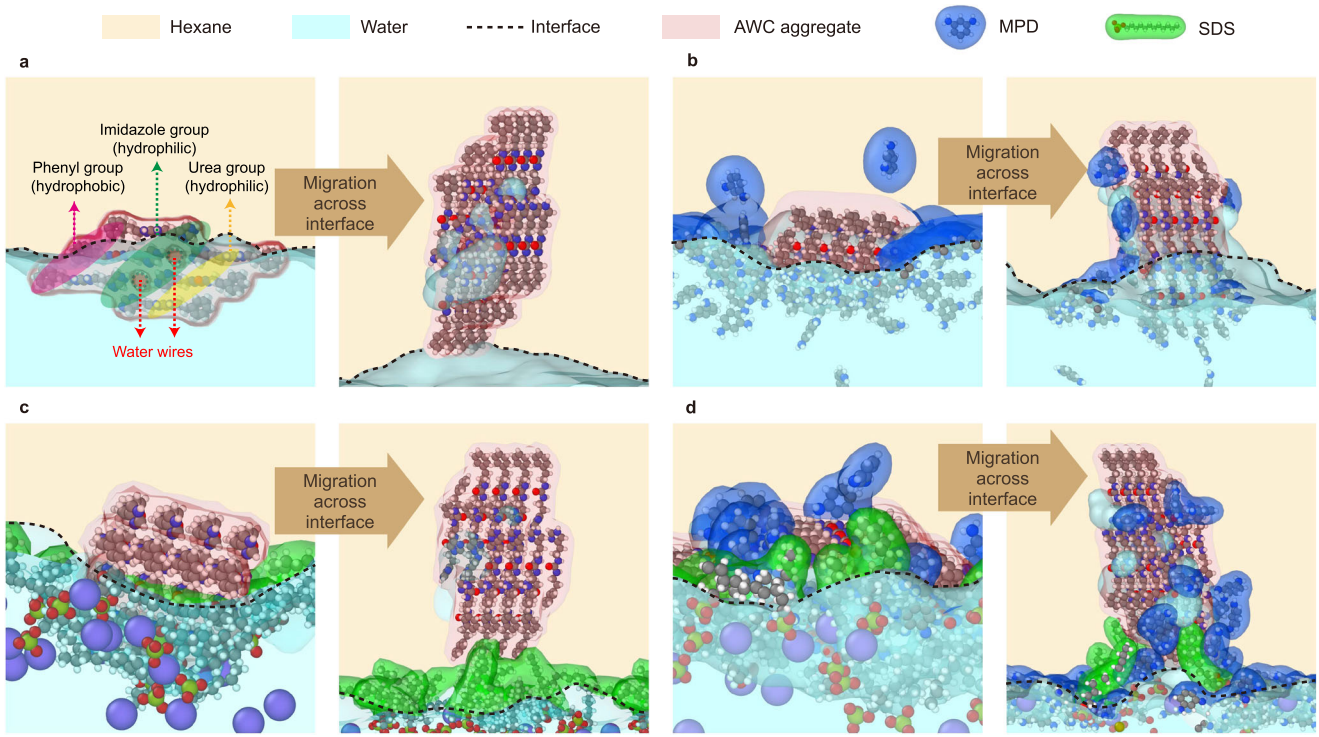

Fig. 6 | MD simulation for the migration of AWC, MPD and SDS during IP. Images show the state of AWC aggregates at the interface (left) and in the organic phase (right). The van der Waals boundaries of different compounds are highlighted by different colors, red for AWC aggregates, light blue for water, dark blue for MPD, and green for SDS. Migration of AWC without the adsorption of MPD (**a**). Migration of AWC with the adsorption of MPD (**b**). Migration of AWC without the adsorption of MPD after SDS was added (**c**). Migration of AWC with the adsorption of MPD after SDS was added (**d**).

For identification, we named the SDS-PA membrane, AW-PA membrane and AWC-SDS-PA membrane as SDS-x membrane, AWC-y membrane and AWC-SDS-z membrane, respectively, where x is the concentration of SDS, y is the concentration of IUP in ethanol, and z is the concentration of IUP in water.

Material characterization

NMR spectroscopy was employed to analyze the sample of IUP compounds, utilizing a Bruker Avance III 600 MHz NMR spectrometer. The spectra were corrected using the solvent dimethyl sulfoxide-d6 (DMSO-d6) as a reference. The crystals were subjected to diffraction analysis on a Bruker D8 venture diffractometer at 293 K during data collection. Using Olex2, the structure was solved with the SHELXT structure solution program using Intrinsic Phasing and refined with the SHELXL refinement package using Least Squares minimization.

The morphology and the thickness of the PA layers were obtained by SEM, TEM and AFM. A 5 nm thick gold coating was sputtered under vacuum conditions (10^{-1} mbar) to obtain the minimum conductivity for reliable SEM information. The PA layer on the surface of TFC membrane was observed by high-resolution scanning electron microscopy (Phenom ProX Desktop SEM) at an accelerating voltage of 15 kV. The membranes were embedded in epoxy resin and subsequently sectioned with an ultrathin slicer (Leica EM KMR3). The membrane cross-sectional morphology was then obtained using a transmission electron microscope (Thermo Scientific Talos F200X STEM). The thickness of the PA layer was measured using AFM (Bruker Dimension Icon). All images within a $5 \times 5\ \mu m^2$ region were captured using the tap mode, with a minimum sampling resolution of 256 points per 256 rows. The PA layer was peeled off from the TFC surface and loaded onto a silicon wafer for testing. Subsequently, the height of the PA layer in relation to the silicon wafer is recorded.

Dynamic light scattering (DLS)

By adding water to an ethanol solution of IUP molecules, AWC aggregates can be formed at the interface of ethanol and water. AWC aggregates can also be obtained by dissolving the IUP molecules in water solution, followed by heating, sonication and cooling to room temperature. The colloid AWC aggregates can be analyzed by DLS testing. DLS testing was performed on a Nanolink S900 Nano Particle Size Analyzer using a quartz cuvette with a 10 mm square aperture at a measurement angle of 90°. The samples were maintained at a temperature of 25 °C for 30 s and then tested in the instrument. The average size was calculated using the hydrodynamic diameter (D_h) values obtained from at least three different measurements. Furthermore, the volume distribution of AWC aggregates was obtained. Unless otherwise specified, the D_h values of AWC aggregates were obtained at 5 min of self-assembly.

Water transport experiments of AWC in liposomes

In this experiment, liposomes were prepared by thin film rehydration and water channels were added by injection method. Briefly, 1.00 mg of a 1/1 molar ratio phosphatidylcholine/cholesterol mixture was dissolved in a chloroform/methanol mixture ($CHCl_3$/MeOH, v/v:1/1). The solution was dried on a rotary evaporator and the residual solvent was removed under high vacuum. After rehydration in 1.00 mL buffer containing 200 mM (6.85 wt/vol%) sucrose and 10.0 mM PBS (pH = 7.2–7.4), the suspension was passed through a 100 nm radial trace-etched polycarbonate filter membrane (Whatman, UK) for 21 passes to obtain monodispersed monolayers of liposomes. IUP dissolved in dimethyl sulfoxide was then added to the liposomes.

Liposomes exposed to a sucrose solution with a concentration of 400 mM exhibited a contraction due to the osmotic pressure exerted by the solution (Supplementary Fig. 17). The changes in the light

scattering signal resulting from liposome contraction were tested at 90° using a kinetic stopped-flow spectrometer. A stopped-flow spectrometer (SFM3000 + MOS450, Claix BioLogic SAS, France) was employed to record the alterations in light scattering at 450 nm, with a measured dead time of 0.500 ms and a test time of 5.00 s. The solution mixture was maintained at a temperature of 20 °C for a period of 30 min prior to exposure to a 400 mM sucrose solution. The data were then fitted as a sum of two exponential functions, and the exponential coefficients were calculated to obtain the initial rate of change in light scattering, k, and the water permeability (P_f), which was calculated using the following expression[41,42]:

$$P_f = \frac{k}{\left(\frac{S}{V_0}\right) \times V_W \times \Delta_{osm}} \quad (1)$$

k represents the initial rate of change in light scattering, expressed as the initial slope of the exponential function fitting equation. The variables S and V_0 correspond to the initial surface area and volume of the liposome, respectively, which are calculated from the liposome particle size. Additionally, V_W denotes the molar volume of water, while Δ_{osm} represents the osmotic pressure.

Membrane performance

All filtration tests were conducted using a laboratory-scale cross-flow system, comprising a high-pressure pump, a feed vessel, and a flat-plate membrane chamber. The effective area of the membrane sample was 57 cm^2. Shut-off and bypass valves cooperatively controlled the operating pressure and system flow, which was monitored by a floating disk rotameter. Temperature was controlled by a circulating chiller connected to a stainless-steel coil immersed in the feed tank.

The feed solution was a 2.00 g/L NaCl solution at a pH of ~7.5. The temperature in the reverse osmosis (RO) system was 20 °C, and the crossflow velocity (averaged across the membrane channel cross-section) was ~0.45 m/s. Each membrane was firstly compacted for 1 h until the pure water flux was steady. Then, the permeation test was implemented at 16.00 bar. All membrane samples were taken in triplicate. Each sample was measured at least three times and then reported as an average with the mean and standard deviation of the performance given. The water permeability (A) and salt rejection (R) of the membranes can be obtained by the following equations:

$$A = \frac{\Delta V}{S \cdot \Delta t \cdot \Delta p} \quad (2)$$

$$R = \left(1 - \frac{C_p}{C_f}\right) \times 100\% \quad (3)$$

$$B = \frac{\Delta V \cdot (1 - R)}{S \cdot \Delta t \cdot R} \quad (4)$$

where A is the water permeability coefficient of the membrane ($L \cdot m^{-2} \cdot h^{-1} \cdot bar^{-1}$), ΔV is the permeate volume (L), S is the effective membrane area (m^2), Δt is the measurement time (h), and Δp is the water pressure difference (bar). R is the salt rejection, C_p is the NaCl concentration of the permeate, and C_f is the NaCl concentration of the feed solution. B is solute permeability coefficient ($L \cdot m^{-2} \cdot h^{-1}$).

Computational simulation

MD simulations were performed using the Large-scale Atomic/Molecular Massively Parallel Simulator[43]. All atoms were treated as charged Lennard-Jones (LJ) sites with parameters taken from the GAFF force field[43,44]. The charges obtained by the AM1-BCC method[45]. The water molecules were described by TIP3P model. The interaction was calculated as the sum of the van der Waals contribution (Lennard-Jones, LJ) and the Coulomb term, with 9 Å and 10 Å being used as the internal and external cutoffs for the LJ interactions. The electrostatic term was computed by taking into account the Ewald method, with the Coulomb force computed at a cutoff of 10 Å. A time step of 1 fs was used in these simulations. More details are listed in the Supplementary Information.

The simulation data for water penetration of the PA layer is used to calculate volumetric flux of water, J_w, and the water permeability, K_w. The formulas for the calculations are provided below.

$$J_w = \frac{M_W}{\rho_w N_A A_{xy}} \frac{\Delta N_p}{\Delta t} \quad (5)$$

where M_W is the molar mass of water, ρ_w is the density of water at 300 K and 1 bar, N_A is Avogadro's constant, A_{xy} is the cross-sectional area of the polyamide domains, N_p is the number of permeating water molecules, and t is the permeation time.

$$K_w = \frac{J_w L}{(P_f - P_p)} \quad (6)$$

where P_f is the pressure in the feed tank, P_p is the pressure in the permeate tank, and L is the thickness of the polyamide domain (z-direction).

Data availability

The experimental data generated in this study are provided in the source data file. MD Trajectories were provided in an additional source data file. Crystallographic data for the structures reported in this article have been deposited at the Cambridge Crystallographic Data Centre, under deposition numbers CCDC 2384618 and 2384619. Copies of the data can be obtained free of charge via https://www.ccdc.cam.ac.uk/structures/. The other data that support the findings of this study are available from the corresponding author on request. Source data are provided with this paper.

Code availability

The codes for simulations performed in this study (MD) are available from the corresponding author upon request.

References

1. Geise, G. M. Why polyamide reverse-osmosis membranes work so well. *Science* **371**, 31–32 (2021).
2. Chowdhury, M. R., Steffes, J., Huey, B. D. & McCutcheon, J. R. 3D printed polyamide membranes for desalination. *Science* **361**, 682–685 (2018).
3. Park, H. B., Kamcev, J., Robeson, L. M., Elimelech, M. & Freeman, B. D. Maximizing the right stuff: The trade-off between membrane permeability and selectivity. *Science* **356**, eaab0530 (2017).
4. Hu X. H. et al. Novel thin-film composite reverse osmosis membrane with superior water flux using parallel magnetic field induced magnetic multi-walled carbon nanotubes. *J. Clean. Prod.* **242**, 118423 (2020).
5. Zhao, C. et al. Polyamide membranes with nanoscale ordered structures for fast permeation and highly selective ion-ion separation. *Nat. Commun.* **14**, 1–9 (2023).
6. Sun, P.-F. et al. Interlayered forward osmosis membranes with Ti_3C_2Tx MXene and carbon nanotubes for enhanced municipal wastewater concentration. *Environ. Sci. Technol.* **55**, 13219–13230 (2021).
7. Wang, X. et al. Robust ultrathin nanoporous MOF membrane with intra-crystalline defects for fast water transport. *Nat. Commun.* **13**, 1–11 (2022).
8. Wen, Y. et al. Metal-organic framework enables ultraselective polyamide membrane for desalination and water reuse. *Sci. Adv.* **8**, eabm4149 (2022).

9. Kaucher, M. S. et al. Selective transport of water mediated by porous dendritic dipeptides. *J. Am. Chem. Soc.* **129**, 11698–11699 (2007).
10. Licsandru, E. et al. Salt-excluding artificial water channels exhibiting enhanced dipolar water and proton translocation. *J. Am. Chem. Soc.* **138**, 5403–5409 (2016).
11. Shen, Y.-xiao et al. Achieving high permeability and enhanced selectivity for angstrom-scale separations using artificial water channel membranes. *Nat. Commun.* **9**, 2294 (2018).
12. Shen, Y. Beating natural proteins at filtering water. *Science* **376**, 698–699 (2022).
13. Shen, J. et al. Fluorofoldamer-based salt- and proton-rejecting artificial water channels for ultrafast water transport. *Nano Lett.* **22**, 4831–4838 (2022).
14. Zhao H., Sheng S., Hong Y., & Zeng H. Proton gradient-induced water transport mediated by water wires inside narrow aquapores of aquafoldamer molecules. *J. Am. Chem. Soc.* **7**, https://doi.org/10.1021/ja5077537 (2014).
15. Chang, H. Y. et al. Water-induced self-assembly of amphiphilic discotic molecules for adaptive artificial water channels. *ACS Nano* **15**, 14885–14890 (2021).
16. Song, W. et al. Artificial water channels enable fast and selective water permeation through water-wire networks. *Nat. Nanotechnol.* **15**, 73–79 (2020).
17. Huang, L. B. et al. Bilayer versus polymeric artificial water channel membranes: Structural determinants for enhanced filtration performances. *J. Am. Chem. Soc.* **143**, 14386–14393 (2021).
18. Di Vincenzo, M. et al. Biomimetic artificial water channel membranes for enhanced desalination. *Nat. Nanotechnol.* **16**, 190–196 (2020).
19. Deng, J.-H. et al. π-π stacking interactions: non-negligible forces for stabilizing porous supramolecular frameworks. *Sci. Adv.* **6**, eaax9976 (2020).
20. Brunsveld, L., Folmer, B. J. B., Meijer, E. W. & Sijbesma, R. P. Supramolecular polymers. *Chem. Rev.* **101**, 4071–4098 (2001).
21. Murail, S. et al. Water permeation across artificial I-quartet membrane channels: from structure to disorder. *Faraday Discuss* **209**, 125–148 (2018).
22. Gan, Q. et al. Demystifying the role of surfactant in tailoring polyamide morphology for enhanced reverse osmosis performance: mechanistic insights and environmental implications. *Environ. Sci. Technol.* **57**, 1819–1827 (2023).
23. Liang, Y. et al. Polyamide nanofiltration membrane with highly uniform sub-nanometre pores for sub-1 Å precision separation. *Nat. Commun.* **11**, 1–9 (2020).
24. Pacheco, F., Pinnau, I., Reinhard, M. & Leckie, J. Characterization of isolated polyamide thin films of RO and NF membranes using novel TEM techniques. *J. Membr. Sci.* https://doi.org/10.1016/J.MEMSCI.2010.04.032 (2010).
25. Di Vincenzo, M. et al. Tunable membranes incorporating artificial water channels for high-performance brackish/low-salinity water reverse osmosis desalination. *Proc. Natl Acad. Sci. USA* **118**, 1–8 (2021).
26. Chen, D., Werber, J., Zhao, X. & Elimelech, M. A facile method to quantify the carboxyl group areal density in the active layer of polyamide thin-film composite membranes. *J. Membr. Sci.* **534**, 100–108 (2017).
27. Mehrabi, M. et al. Enhanced negative charge of polyamide thin-film nanocomposite reverse osmosis membrane modified with MIL-101(Cr)-Pyz-SOH3. *J. Membr. Sci.* **664**, 121066 (2022).
28. Zhao, Y., Wang, Y.-N., Lai, G. S., Torres, J. & Wang, R. Proteoliposome-incorporated seawater reverse osmosis polyamide membrane: Is the aquaporin water channel effect in improving membrane performance overestimated? *Environ. Sci. Technol.* **10**, 5179–5188 (2022).
29. Zhao, Q., Zhao, D. L. & Chung, T.-S. Thin-film nanocomposite membranes incorporated with defective ZIF-8 nanoparticles for brackish water and seawater desalination. *J. Membr. Sci.* **625**, 119158 (2021).
30. Ge, M. et al. Highly antifouling and chlorine resistance polyamide reverse osmosis membranes with g-C3N4 nanosheets as nanofiller. *Sep. Purif. Technol.* **258**, 117980 (2021).
31. Shao, F. et al. Highly improved chlorine resistance of polyamide reverse membrane by grafting layers of graphene oxide. *Sep. Purif. Technol.* **254**, 117586 (2021).
32. Zhang, D. et al. Preparation of thermally stable 3-glycidyloxypropyl-POSS-derived polysilsesquioxane RO membranes for water desalination. *J. Membr. Sci.* **668**, 121213 (2023).
33. Zhao Q. P., Zhao D. L., & Chung T. S. Nanoclays-incorporated thin-film nanocomposite membranes for reverse osmosis desalination. *Adva. Mater. Interfaces* **7**, 1902108 (2020).
34. Helgason, T., Awad, T. S., Kristbergsson, K., McClements, D. J. & Weiss, J. Effect of surfactant surface coverage on formation of solid lipid nanoparticles (SLN). *J. Colloid Interface Sci.* **334**, 75–81 (2009).
35. Kvítek, L. et al. Effect of surfactants and polymers on stability and antibacterial activity of silver nanoparticles (NPs). *J. Phys. Chem. C* **112**, 5825–5834 (2008).
36. Zhang, A., Zhu, J., Han, S., Zhang, Y. & Van der Bruggen, B. Finely regulated polyamide membranes with rapid water transport for low-pressure precise nanofiltration. *J. Membr. Sci.* **662**, 120987 (2022).
37. Zhao, A. et al. Incorporation of silver-embedded carbon nanotubes coated with tannic acid into polyamide reverse osmosis membranes toward high permeability, antifouling, and antibacterial properties. *ACS Sustain. Chem. Eng.* **9**, 11388–11402 (2021).
38. Tang, Y., Yu, H., Xing, Y., Gao, C. & Xu, J. Microstructure and desalination performance of polyamide membranes interfacially regulated via single-side post-modified CNTs networks. *Desalination* **482**, 114408 (2020).
39. Wang, D. et al. Probing diffusion of single nanoparticles at water–oil interfaces. *Small* **7**, 3502–3507 (2011).
40. Shen, Q. et al. When self-assembly meets interfacial polymerization. *Sci. Adv.* **9**, eadf6122 (2023).
41. Borgnia, M. J., Kozono, D., Calamita, G., Maloney, P. C. & Agre, P. Functional reconstitution and characterization of AqpZ, the E. coli water channel protein11Edited by W. baumeister. *J. Mol. Biol.* **291**, 1169–1179 (1999).
42. Zeidel, M. L., Ambudkar, S. V., Smith, B. L. & Agre, P. Reconstitution of functional water channels in liposomes containing purified red cell CHIP28 protein. *Biochemistry* **31**, 7436–7440 (1992).
43. Wang, J., Wang, W., Kollman, P. A. & Case, D. A. Automatic atom type and bond type perception in molecular mechanical calculations. *J. Mol. Graph. Model.* **25**, 247–260 (2006).
44. Wang, J., Wolf, R. M., Caldwell, J. W., Kollman, P. A. & Case, D. A. Development and testing of a general amber force field. *J. Comput. Chem.* **25**, 1157–1174 (2004).
45. Jakalian, A., Jack, D. B. & Bayly, C. I. Fast, efficient generation of high-quality atomic charges. AM1-BCC model: II. Parameterization and validation. *J. Comput. Chem.* **23**, 1623–1641 (2002).

Acknowledgements

This work was supported by National Nature Science Foundation of China (52270084, J.W.) and Central Universities outstanding youth team project of CUMTB (2023YQTD03, J.W.). The authors thank Research Center for Eco-Environmental Sciences (RCEES), Chinese Academy of Sciences (CAS) for help with water transport experiments of AWC.

Author contributions

J.W. conceived the project and designed the experiments. Y.L. fabricated the membranes, performed XRD and XPS analysis, and MD simulations. X.X. performed NMR characterization. C.W. and H.Y. designed and performed the filtration experiments and MPD diffusion

experiments. W.W. and Y.G. performed SEM, AFM, and TEM experiments. C.Z. performed the estimation of water permeability of membrane with Maxwell equation. J.W. wrote the manuscript with input from all authors. All authors discussed the results and commented on the manuscript.

Competing interests
The authors declare no competing interests.

Additional information
Supplementary information The online version contains supplementary material available at https://doi.org/10.1038/s41467-025-59726-x.

Correspondence and requests for materials should be addressed to Jianbing Wang.

Peer review information *Nature Communications* thanks Xuan Zhang and the other, anonymous, reviewer(s) for their contribution to the peer review of this work. A peer review file is available.